Generalized half-center oscillators with short-term synaptic plasticity

Preprint *in* PHYSICAL REVIEW E · May 2020

DOI: 10.1103/PhysRevE.102.032406

4 authors:

Valentina Baruzzi
Università degli Studi di Genova
7 PUBLICATIONS **7** CITATIONS
SEE PROFILE

Matteo Lodi
Università degli Studi di Genova
38 PUBLICATIONS **252** CITATIONS
SEE PROFILE

Marco Storace
Università degli Studi di Genova
186 PUBLICATIONS **1,882** CITATIONS
SEE PROFILE

Andrey Shilnikov
Georgia State University
212 PUBLICATIONS **3,984** CITATIONS
SEE PROFILE

Generalized half-center oscillators with short-term synaptic plasticity

V. Baruzzi,[1] M. Lodi,[1] M. Storace,[1] and A. Shilnikov[2]

[1]*Department of Electrical, Electronics and Telecommunication Engineering and Naval Architecture, University of Genoa, 16145 Genoa, Italy*

[2]*Department of Mathematics and Statistics, Neuroscience Institute, Georgia State University, Atlanta, Georgia 30303, USA*

(Received 7 May 2020; accepted 24 August 2020; published 10 September 2020)

How can we develop simple yet realistic models of the small neural circuits known as central pattern generators (CPGs), which contribute to generate complex multiphase locomotion in living animals? In this paper we introduce a new model (with design criteria) of a generalized half-center oscillator, (pools of) neurons reciprocally coupled by fast/slow inhibitory and excitatory synapses, to produce either alternating bursting or other rhythmic patterns, characterized by different phase lags, depending on the sensory or other external input. We also show how to calibrate its parameters, based on both physiological and functional criteria and on bifurcation analysis. This model accounts for short-term neuromodulation in a biophysically plausible way and is a building block to develop more realistic and functionally accurate CPG models. Examples and counterexamples are used to point out the generality and effectiveness of our design approach.

DOI: 10.1103/PhysRevE.102.032406

I. INTRODUCTION

Central pattern generators (CPGs) are small neural circuits that can autonomously (i.e., in the absence of sensory feedback or higher motor planning centers inputs) produce various rhythmic patterns of neural activity [1]. They bear a fundamental function in both invertebrate and vertebrate animals as they determine multiphase locomotion—the innate motor behavior that requires sequential activation of body muscles in a coordinated way [2]. Various approaches to the modeling of CPGs and CPG-inspired control systems have been explored in the last decades [3–7]. Recently, new methods have been proposed to reduce large models of detailed neural networks to smaller CPG circuits, trading off biological plausibility and complexity of the model [3,4,8–10].

Although CPGs function autonomously, their activity is modulated through the influence of hierarchically higher areas, which can, for example, prompt transitions between gaits [11–13]. A single gait in a typical CPG model is obtained by fixing the connectivity. By contrast, to generate multiple gaits the CPG connections between constituent neurons are typically changed acting on the synaptic weights to model the control action of the brainstem [7–9,14]. The modulation from higher areas that controls the synchronization between the CPG neurons, and thus triggers gait switches, is conveniently integrated in CPG models to directly affect the synaptic conductance strengths. However, in real CPGs changes in conductance values are the result of long-term synaptic plasticity, and therefore it is hardly a cause for quick gait switches, which can instead be accounted for more realistically by short-term neuromodulation. Indeed, most natural CPGs exhibit patterns of functional connectivity between neurons or synchronized clusters of neurons that can undergo spontaneous fluctuations and be highly responsive to perturbations, e.g., induced by sensory input or cognitive tasks, on a timescale of milliseconds or hundreds of milliseconds, respectively, thus ensuring robustness and stability. This short-term neuromodulation lacks in most CPG models.

One of the pivotal building blocks of many CPGs is a half-center oscillator (HCO). The HCO-concept is widely used to model two synchronous pools of neurons reciprocally inhibiting each other to produce stable rhythmic alternation in animal locomotion [15,16]. This basic structure has been largely studied from both biological and nonlinear dynamics standpoints. For example, in Refs. [17–20] transitions between stable synchronous states in the HCO occur by changing directly synaptic weights and time constants, whereas in Ref. [21] a large database of HCO models is swept using a brute-force approach, without a focus on gait transitions. While the importance of an interplay between inhibitory and excitatory coupling has already been outlined [17], the thorough understanding of its functional role for determining multiple states or patterns in such neural networks and how transitions between them may stably occur remains yet insufficient. Moreover, there is the growing evidence that (i) post-synaptic potential (PSP) summation increasing with the spike frequency in the pre-synaptic cell is a crucial factor for stable functioning of some CPGs [22–25], while other experiments indicate that (ii) the activity of some synapses is barely affected by the spike frequency [7].

In this paper, we propose a generalized half-center oscillator (gHCO) composed of two neurons or of two neural pools that are coupled reciprocally by excitatory synapses, in addition to the standard HCO's reciprocally inhibitory synapses. We show that this circuitry warrants a more biologically plausible mechanism of short-term plasticity to implicitly control the phase-lag between the gHCO cells by varying their spike frequency through sensory drive or external currents, rather then directly manipulating the synaptic

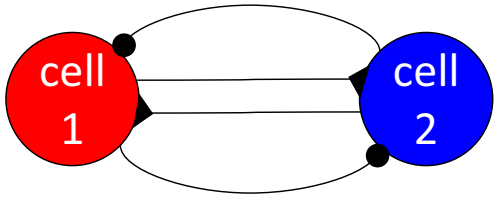

FIG. 1. gHCO neural circuit with inhibitory (denoted with ► ◄) and excitatory (●) synapses reciprocally coupling two oscillatory cells.

conductance strengths. By doing so, we show how spike-frequency dependent synapses can themselves dynamically control the rhythmic outcomes of the gHCO from in-phase bursting to antiphase bursting and vice versa, without changing time constants and conductances. This is an aspect that has not been studied fully in the past literature and is a novelty of our manuscript. Moreover, we are focused on obtaining synchronization regimes other than phasic and antiphasic, with different time lags between cells and hence different gaits, keeping the time constants fixed and changing the spike frequency. The mixed excitatory/inhibitory synapses bring exactly this advantage, which is not already qualitatively accounted for by inhibitory-induced synchronization. Finally, we show how to calibrate the gHCO parameters (i.e., cellular and synaptic parameters) to obtain the desired behaviors, also carrying out a numerical bifurcation analysis.

II. THE GHCO AND ITS DESIGN CONSTRAINTS

The proposed generalized half-center oscillator is shown in Fig. 1. It is made of two neurons or two neural pools, coupled by both excitatory (marked by a black circle) and inhibitory (marked by a black triangle) synapses.

There are a few simple constraints that neurons and synapses must meet for the circuit to generate stably the desired rhythmic outcomes: (a) both neurons are endogenous bursters with (b) the spiking voltage range above the hyperpolarized voltage (i.e., they do not *undershoot* [26]) within each burst, while (c) the mean spike frequency can be controlled. The gHCO bursters are coupled by (d) slow synapses with PSP summation whose strength increases with the growing spike frequency in presynaptic cells, as well as by (e) fast synapses without PSP summation.

In what follows, both gHCO cells are represented by the Hodgkin-Huxley (HH) type model of the thalamic reticular neuron [27,28] (see Appendix). This slow-fast model with seven state variables can exhibit endogenous bursting activity of alternating trains of fast action potentials with long quiescent intervals, as depicted in Fig. 2. The dynamics of the membrane potential V_j and of the voltage-dependent state variables (the vector $\mathbf{y}_j$) are governed by a generic set of HH-like equations,

$$\frac{d}{dt}\begin{bmatrix} V_j \\ \mathbf{y}_j \end{bmatrix} = \begin{bmatrix} -\sum_k I_k + I_j^{\text{syn}} \\ f(V_j, \mathbf{y}_j) \end{bmatrix}, \quad \text{where } j = 1, 2, \qquad (1)$$

where $f(V_j, \mathbf{y}_j)$ is a vector function describing $\mathbf{y}_j$-dynamics; in particular, each f component for the HH gating variables is

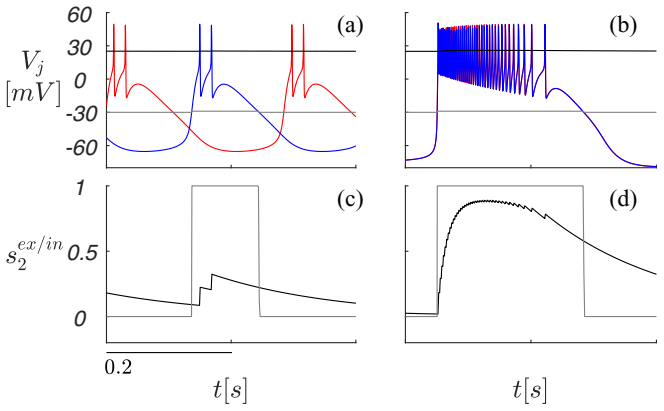

FIG. 2. Asymptotic antiphase (a) and synchronous (b) bursting voltage traces V_1 (red) and V_2 (blue) at $I_c = -0.43$ and 0.13, respectively, in gHCO (1–3), superimposed with excitatory/inhibitory thresholds θ (horizontal lines) at 25 and -30 mV. (c, d) Synapse dynamics: fast modulatory $s_2^{\text{in}}(t)$ (gray) vs. slowly summating/decaying $s_2^{\text{ex}}(t)$ (black). See the Appendix for parameters.

a logistic function. In addition to intracellular currents, $\sum_k I_k$ includes a further external contribution, namely a control current I_c acting essentially on the spike frequency within bursts. For the given model, bursting activity occurs when $I_c \in [-0.43,\ 0.13]\,[\frac{\mu\text{A}}{\text{cm}^2}]$, with the mean intraburst interval decreasing from 15.36 to 4.13 ms. The term I_j^{syn} is the incoming mixed, excitatory/inhibitory synaptic current originating from the ith cell onto the jth, postsynaptic cell:

$$I_j^{\text{syn}} = g^{\text{ex}}(E^{\text{ex}} - V_j)s_i^{\text{ex}} + g^{\text{in}}(E^{\text{in}} - V_j)s_i^{\text{in}}, \qquad (2)$$

where $E^{\text{ex/in}}$ are the reversal potentials for excitatory/inhibitory synapses and $0 \leqslant s_i^{\text{ex/in}} \leqslant 1$ is the activation or neurotransmitter release rate of the synapse, excitatory ($V_j < E^{\text{ex}}$) or inhibitory ($V_j > E^{\text{in}}$). For the slow synapses with PSP summation we employ a first-order dynamic synapse [29–31]. The dynamic evolution of its activation rate is governed by the following equation

$$\frac{ds_i}{dt} = \alpha\,(1 - s_i)f_\infty(V_i) - \beta s_i, \quad f_\infty = \frac{1}{1 + e^{-\nu(V_i - \theta)}}, \qquad (3)$$

where θ is the synaptic voltage threshold, whereas α and β are dimensional coefficients weighting the raise and decay terms, respectively. To model the static synapses without PSP summation we employ the fast threshold modulation (FTM) paradigm [32] using the sigmoidal function: $0 \leqslant s_i = f_\infty(V_i) \leqslant 1$, with θ being below the spiking voltage threshold.

To illustrate the contrasting properties of these synapse models, we refer to Fig. 2, showing the bursting voltage traces V_1 (red) and V_2 (blue) and the synaptic activation dynamics, fast $s_2^{\text{in}}(t)$ (gray) and slow $s_2^{\text{ex}}(t)$ (black) at the edge of the I_c bursting interval. Observe that the neurotransmitter release rate $s_2^{\text{in}}(t)$ of the FTM synapse (1) is maximized as soon as the voltage $V_2(t)$ in the presynaptic cell overcomes the synaptic threshold θ^{in} [indicated by the gray lines in Figs. 2(a) and 2(b)], (2) remains constant regardless of the spike frequency, and (3) vanishes with the burst termination.

In contrast, the low spike frequency [Figs. 2(a) and 2(c)] barely activates the slow synapse [see $s_2^{\rm ex}(t)$] that at high spike frequency [Figs. 2(b) and 2(d)] exhibits the profound PSP build up; the ascending rate is ruled by $\alpha > 0$, and the exponential decay due to $\beta > 0$ starts after the voltage lowers below θ. As stated above, the strenght of the fast synapse does not depend on spike frequency, whereas the strength of the slow synapse does. Consequently, changing the spike frequency through an incoming current allows to modify the ratio between inibition and exhitation strengths and thus influences the phase lag between the neurons.

III. PARAMETER CALIBRATION

The neuron and synapse models (1–3) are calibrated to physiologically plausible values to meet the above requirements (a)–(e) and to ensure a smooth and reversible transition from antiphase to in-phase bursting by way of stable intermediate phase lags as the spike frequency changes due to I_c variations. Just to clarify things, let us consider the dynamics of the gHCO with fast inhibitory and slow excitatory synapses, whose thresholds are set at $\theta^{\rm in} = -30$ and $\theta^{\rm ex} = 25$ mV, respectively. As such, the inhibitory synapses without PSP summation (de)activate quickly and their strengths remain constant during each burst regardless of the spike frequency. In contrast, the slow excitatory synapses exhibit PSP summation that becomes stronger with an increase of the spike frequency.

Figure 2 shows that at the low end $I_c = -0.43$ of the bursting region, near the transition to the hyperpolarized quiescence, the gHCO neurons oscillate in antiphase with the smallest number of spikes per burst and lowest spike frequency [Figs. 2(a) and 2(c)], whereas on the opposite side at $I_c = 0.13$ the neurons burst in phase with a larger number of spikes per burst and with much higher spike frequency [Figs. 2(b) and 2(d)]. Changing the value of I_c changes the strength of the excitatory synapses, and hence the proportion between inhibition and excitation that repel the gHCO neurons or attract them to each other, respectively. The *phase-lag* Δ between burst initiations in the neurons [33–35] allows quantifying the phase-locked states produced by the gHCO. The definition of phase-lag Δ assumes that isolated or coupled neurons maintain relatively close temporal characteristics and each one evolves on a structurally stable periodic orbit in the state space of the corresponding model. The phase variable $\phi_j(t)$, defined modulo 1, indicates the position on the periodic orbit of the jth neuron. Consequently, the phase lags between burst initiations in a network of two neurons can be described by the state variable $\Delta = \phi_2 - \phi_1$. The time evolutions of this state variable, being quite complex due to nonlinear interactions, can be determined through numerical simulations, in which $\phi_j(t)$ is reset to 0 when the voltage V_j increases above some synaptic threshold V_{th} at times $t_j^{(q)}$. We compute the phase lags between coupled cells in a discrete set of time instants as

$$\Delta^{(q)} = \frac{t_2^{(q)} - t_1^{(q)}}{t_1^{(q)} - t_1^{(q-1)}}, \quad \text{mod } 1. \tag{4}$$

In our simulations, we set $V_{\rm th} = -30$ mV.

In the case of synchronous or in-phase bursters, $\Delta = 0$ (or $\Delta = 1$). When they burst in alternation, with $\Delta = 0.5$, we say that they are in antiphase. The intermediate values of Δ correspond to patterns transitional between the in- and antiphase states generated by the gHCO. Their physiological relevance is related to the different gaits that one can obtain using the gHCO as basic element. For instance, there are quadruped gaits characterized by phase lags not corresponding to in-phase (i.e., phase lag of 0 or 1) or antiphase (i.e., phase lag of 0.5) synchronization [36,37]: the gallop, indeed, requires a phase lag of 0.1 between right fore and hind legs and of 0.6 between left fore and hind legs; the walk requires a phase lag of 0.25 between left fore and hind legs and of 0.75 between left fore and right hind legs. The possibility of having different phase lags at steady state by changing I_c should allow obtaining all these gaits, as shown in our previous works [9,14].

The bifurcation analysis of the system (1–3) was carried out using the computational toolbox CEPAGE [38]. Since we want the gHCO to transition smoothly from antiphase regime to in-phase regime varying I_c, we need the proportion between inhibition and excitation to be significantly different for the two values of I_c at the edges of its range. To this end, we seek maximum difference in the mean values of $s_i^{\rm ex}$ (over one period) at the two extreme values of I_c, i.e., -0.43 (antiphase pattern) and 0.13 (in-phase bursting). We set the numerical values of $\theta^{\rm ex}$, α and β according to this principle, running a set of simulations over a grid of parameter values: $\theta^{\rm ex} = \{10, 25\}$, 10 evenly spaced values of $\alpha \in [0.05, 1]$ and 10 evenly spaced values of $\beta \in [0.005, 0.1]$. The considered values of $\theta^{\rm ex}$ indicate voltage levels representative of two different conditions: at $\theta^{\rm ex} = 10$ each spike appears broader, namely V_j stays above $\theta^{\rm ex}$ for a longer time window; at $\theta^{\rm ex} = 25$ each spike appears narrower, namely V_j stays above $\theta^{\rm ex}$ for a shorter time period. We choose the parameter setting that provides maximum difference in the mean values of $s_i^{\rm ex}$ for the two extreme values of I_c (see Appendix B). We re-emphasize that the values of $\theta^{\rm ex}$, α, and β, chosen as explained above, remain fixed during all simulations, according to our initial assumptions: we want to study how spike-frequency dependent synapses can *themselves* dynamically control the rhythmic outcomes of the gHCO from in-phase bursting to antiphase bursting and vice versa, without changing time constants and conductances and passing through intermediate steady-state values of Δ. Following the same line of reasoning, the synaptic conductances $g^{\rm in/ex}$ are set to constant values, which are chosen to obtain antiphase synchronization for low spike frequency, condition in which the mean value of $s_i^{\rm ex}$ is minimum, and in-phase synchronization for high spike frequency, condition in which the mean value of $s_i^{\rm ex}$ is maximum. If the value of $g^{\rm ex}$ is too high, then the neurons will always manifest in-phase steady state behavior no matter the value of I_c, whereas if the value of $g^{\rm in}$ is too high, they will always stabilize in antiphase. We set $g^{\rm in/ex}$ tweaking their values through a set of simulations for the two extremes of the I_c range, reaching the desired ratio $g^{\rm in}/g^{\rm ex}$ that gives antiphase synchronization for minimum I_c and in-phase synchronization for maximum I_c.

The results are summarized in Fig. 3, and reveal the dependence of the phase-lag Δ on the I_c-current, and hence explicitly on the spike frequency within bursts. As expected,

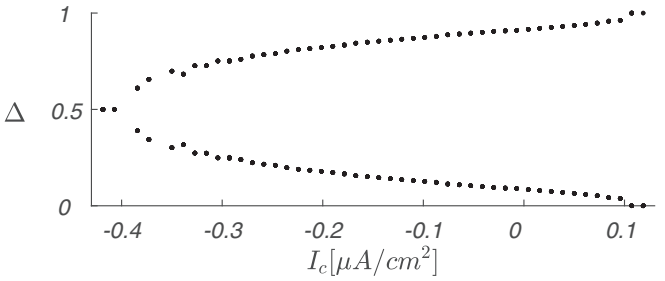

FIG. 3. Bifurcation diagram showing how the phase-lag Δ between the gHCO neurons is affected by the current I_c; here, 30 initial Δ-values were sampled evenly between 0.05 and 0.95 for each of the 50 I_c-values. Parameters listed in the Appendix.

at low I_c-values between -0.43 and -0.40, the fast reciprocal inhibition within the gHCO dominates and makes its neurons burst in alternation with $\Delta = 0.5$. As the I_c-current is increased, the spike frequency raises, which in turn makes the slow excitatory synapses strength increase, on average. With larger I_c values, the reciprocal excitation gradually prevails over the reciprocal inhibition, which gives rise to the smooth onset of the stable in-phase bursting in the gHCO. This is revealed in the bifurcation diagram with a characteristic pitchfork shape of the dependence of the phase-lag Δ on the I_c-current. We also note that this diagram has been obtained by making a multishooting for each parameter value, namely, running sufficiently many (30 in our case) trials with initial conditions equally spaced in the Δ range [0,1]. This is a direct indication that there is no hysteresis and therefore the absence of multistability or the coexistence of anti- and in-phase bursting for the same parameter values, and that the transition between activity rhythms is continuous and reversible. We would like to re-emphasize that the maximal synaptic conductances $g^{\text{in/ex}}$ in Eq. (2) once set are not changed, and the transition is solely determined by the gradual increase/decrease of the mean s_i^{ex}-value caused by the spike frequency variations in the gHCO neurons.

IV. COUNTEREXAMPLES

The proposed gHCO concept can fall apart whenever one or more of the conditions on the neuron and synapse models are not fulfilled. If the bursting condition (a) is broken, then the approach is no longer applicable. Two neurons, spiking in isolation, can burst in alternation due to reciprocal inhibition, but not through reciprocal excitation, which makes both even more synchronously depolarized with a higher frequency. If the neurons undershoot [condition (b)], which is typical for elliptical bursters [40] [see Fig. 4(a)], then the choice of the inhibitory threshold θ^{in} to warrant evenly constant activation s_i^{in} requires additional considerations. Indeed, this choice can result in less robust dynamics of the gHCO, due to inhibition-excitation competition [see Fig. 4(b)]. Condition (c), outlining the importance of being able to control spike-frequency and not only burst duration of the pre-synaptic cell, is quite crucial for obtaining many stable values of Δ. To point out its significance, we employ the exponential integrate-and-fire (eIF) neuron model [41], where an external current I_{ext} primarily controls the burst duration with insignificant spike-frequency

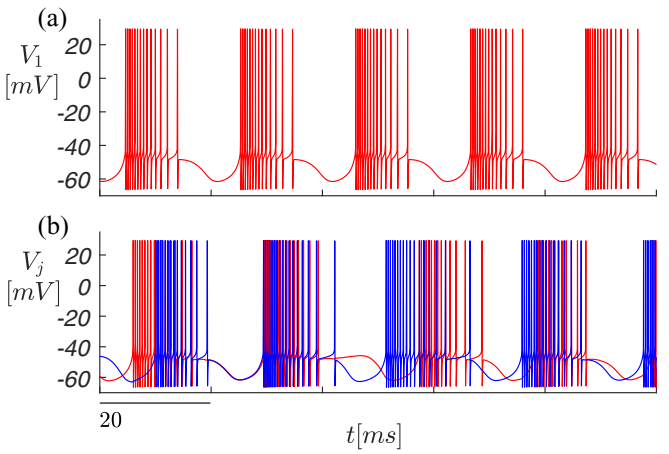

FIG. 4. (a) Asymptotic bursting voltage trace with undershoot produced by the Plant neuron model [39,40]. (b) Voltage traces produced by the gHCO with two coupled Plant neurons. See the Appendix for parameters.

variations, as shown in Fig. 5(a). In this scenario, the activation of both inhibitory and excitatory synapses is mainly determined by the burst duration in the eIF neurons, and thus I_{ext} variations can only cause proportional changes in the average excitation (s_i^{ex}) and inhibition (s_i^{in}). As a result, the ratio between excitation and inhibition does not vary significantly within the given I_{ext} range, and thus, for fixed conductances and time constants, the phase lag remains practically unaltered, as shown in Fig. 5(b). Conversely, changing the parameter g_e of the eIF neuron model significantly modifies the spike frequency, and the corresponding bifurcation diagram has the characteristic pitchfork shape shown in Fig. 6, as expected. However, the parameter g_e is a conductance, and thus is not a realistic control parameter, according to our guidelines.

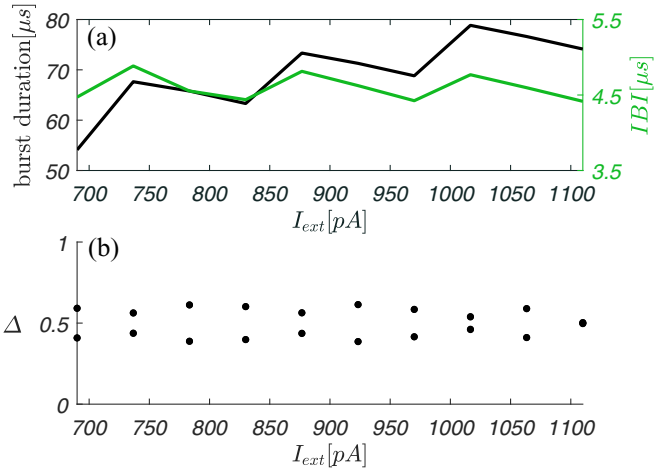

FIG. 5. (a) Mean values (over 5 s) of the IBI (green line) and the burst duration (black line) plotted against I_{ext} for the exponential IF-model [41]. Corresponding bifurcation diagram for the phase lag Δ between the cells in the gHCO, in which each cell is an exponential IF-model (b).

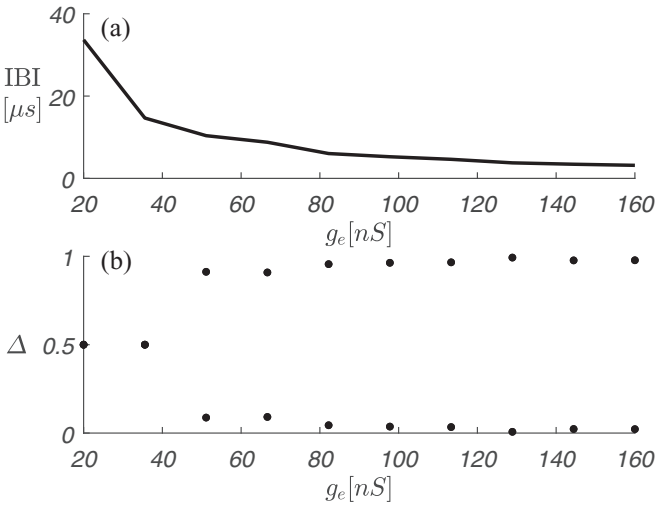

FIG. 6. (a) Mean values (over 5 s) of the IBI plotted against g_e for the exponential IF-model [41]. Corresponding bifurcation diagram for the phase lag Δ between the cells in the gHCO, in which each cell is an exponential IF-model (b).

Condition (d) follows condition (c), as the synaptic threshold θ, for the slow synapses, has to be within the spike voltage range of the pre-synaptic neuron and the dynamics is to be slow enough to allow $s_i(t)$ to grow and the synapse to exhibit PSP summation. Condition (e) guarantees that the activation of the fast synapse does not exhibit PSP summation and hence does not change due to spike frequency variations in the pre-synaptic neuron.

V. TOWARD A LOCOMOTION CPG

As the gHCO often happens to be a CPG building block, we discuss some solutions ensuring that both the phase lags and the burst frequency are consistent for the modeled gaits. For instance, in left-right alternation of the mouse locomotion, a phase lag $\Delta = 0.5$ occurs at low burst frequencies (walk and trot gaits), whereas a phase lag Δ close to 0 (or to 1, equivalently) occurs at high burst frequencies (gallop and bound gaits) [14,36,37]. Recall that the thalamic reticular neuron model in isolation exhibits high frequency bursting at small I_c-values and slow bursting at greater I_c-values. Therefore, for the gHCO built with such models to produce in-phase/antiphase synchronization at high/low burst frequencies for the desired gaits, the time-scale of the synapses in its circuitry should be swapped: slow inhibitory synapses with PSP summation and fast excitatory ones without PSP summation, see the Appendix for details. Moreover, we use a modified version of the first-order synapse to model slow inhibitory synapses. The dynamics of its activation is governed by the following equation:

$$\frac{ds_i}{dt} = \alpha\, s_i\,(1 - s_i) f_\infty(V_i) - \beta s_i, \tag{5}$$

where the new multiplicative term delays and hence slows down the synaptic activation for low spike-frequency in the pre-synaptic neuron; the synapse remains inactive near $I_c = -0.43$. The synapse given by Eq. (5) maintains a greater

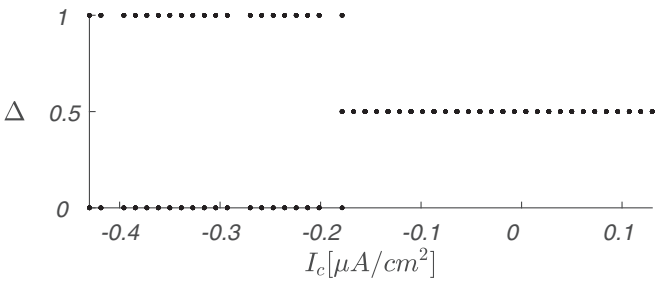

FIG. 7. Bifurcation diagram showing the flat-even phase-lags, $\Delta = \{0,\ 1\}$ (in-phase) and $\Delta = 0.5$ (antiphase), between the bursters plotted against the current I_c for the gHCO with slow inhibitory and fast excitatory synapses; here, 30 initial Δ-values were sampled evenly between 0.05 and 0.95 for every I_c value out of 50. Parameters listed in the Appendix.

contrast in the mean s_i-values corresponding to the low and high ends of the bursting I_c-range for the given neuron model. The results are summarized in Fig. 7, representing the bifurcation diagram for this gHCO. It demonstrates that the gHCO bursters oscillate robustly in-phase ($\Delta = \{0,\ 1\}$) for negative I_c-values and transition to the stable antiphase ($\Delta = 0.5$), phase-locked state as the drive is increased above -0.2. Despite the abrupt jump in the bifurcation diagram, the time evolution between in-phase and antiphase bursting occurs smoothly [see Fig. 8(b), which shows a fragment of the smooth time transition from in- to antiphase bursting] as the control current I_c is step-wise increased from -0.43 to 0.13 [see the dashed green lines in Fig. 8(a)].

Notice that the abrupt transition in Fig. 7 means that with this configuration we cannot generate every possible gait, but only the ones that require in-phase or antiphase synchronization. This is a suboptimal situation, of course, to which we aim only when a specific neuron model fails in hitting the original target, which is finding a bifurcation diagram like that shown

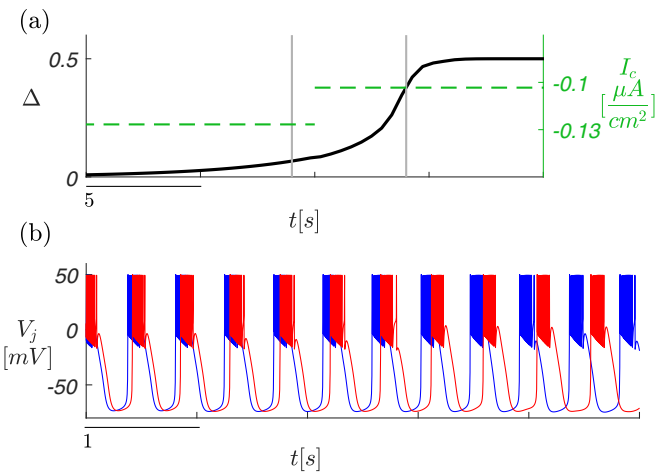

FIG. 8. (a) Time evolution of the phase lag Δ between the gHCO cells (black line) in response to step-wise changes of I_c (green dashed lines); I_c increased over 25 steps from -0.43 to 0.13, only the time window in which Δ transition occurs is shown. (b) Voltage traces progressing from in-phase to antiphase bursting within the time window bounded by the grey vertical lines in panel (a).

in Fig. 3, with the smooth transition between antiphase and fully in-phase steady-state dynamics as a function of I_c.

VI. CONCLUDING REMARKS

We developed a generalized HCO-model with a short-term plasticity mechanism, which accounts for short timescale gait transitions induced by sensory input or cognitive tasks. The proposed concept is based on simple constraints (i) subjecting models for cells and synapses and (ii) optimizing the trading-off between physiological plausibility and model functionality. The generality of our approach suggests that it will be applicable for other biologically plausible and phenomenological models of endogenous (square-wave) bursters, and for other dynamic synapse models.

Many previous works on the phasic/antiphasic synchronization of neurons or groups of neurons analyzed the influence of synaptic changes on the circuit dynamics. In Ref. [20] the authors study the synchronization of spiking cells coupled by slow inhibitory synapses such that the inhibition decay is about equal to (or longer than) the interspike interval, controlled by the synaptic time constant in the FTM model. This is a well-known result [42] due to a small initial phase difference, falling in a tight window that lets both cells spike together. Otherwise, either active cell suppresses the other by long lasting inhibition that does not let the latter spike. When the synapses have smaller time constants and smaller weights, the network does not produce any steady pattern of activity. This is different from our case, where the convergence to phasic or antiphasic steady state is independent of the initial state, and is not suitable for CPGs that are supposed to be reliable pattern generators with preset qualities. Moreover, we want to obtain steady-state phase lags other than in-phase and antiphase. Finally, in our network, we fix all synaptic conductances and constants.

In Ref. [18] the same approach is used, with a pair of reciprocally coupled endogenous bursters that oscillate in antiphase as long as the inhibition is set short. For higher values of the synaptic time constant, both cells burst in phase provided that their initial states are close and the inhibitory current decays slowly and lasts as long as the interburst interval. In the discussion the authors mention "The duration of the interburst interval will control the time of burst initiation, and thus the relative phase of bursting in the postsynaptic and presynaptic neurons." This strategy is far from our approach, since, as shown in the counterexamples, the burst duration and the interburst interval are not key elements in determining the stable phase differences.

In Ref. [19], a pair of IF cells are coupled by inhibitory and electrical synapses. The conclusion is that increasing electrical coupling makes the cells spike in sync, if prior they spiked in antiphase. Again, the authors change the coupling parameters to ensure phasic or antiphasic synchrony. It is well known that repulsive/inhibitory coupling in general either makes the cells fire in antiphase or makes one cell get shut down, whereas both electrical and excitatory coupling make the cells fire together.

Our paper is not based on the above findings. Its focus is on how spike-frequency dependent synapses can themselves dynamically control the rhythmic outcomes of the gHCO from in-phase bursting to antiphase bursting and vice versa, without changing time constants and conductances. Moreover, we are focused on obtaining (owing to the excitatory synapses and keeping the time constants fixed) all possible time lags between cells and hence gaits that require synchronization regimes other that phasic and antiphasic.

ACKNOWLEDGMENTS

We acknowledge J. Scully's contribution to the concept and development of the synapse model Eq. (5). A.S.'s research was partially funded by the NSF Grant No. IOS-1455527. M.S. and A.S. conceptualized the work; V.B. and M.L. conducted the experiments.

APPENDIX A: NEURON MODELS

1. Thalamic reticular neuron model

The thalamic reticular neuron model [27,28] is defined by the following state equations:

$$\begin{aligned}\frac{dV}{dt} &= \frac{-I_T - I_L - I_{\rm Na} - I_{\rm K} - I_c + I^{\rm syn}}{C}\\ \frac{d{\rm Ca}}{dt} &= -\frac{kI_T}{2Fd} - \frac{K_T{\rm Ca}}{{\rm Ca}+K_d}\\ \frac{dy}{dt} &= \frac{y^\infty - y}{\tau_y} \quad y=\{h,m,n,m_T,h_T\}\end{aligned} \tag{A1}$$

where V is the membrane potential of the neuron; the ion currents I_T (calcium), $I_{\rm Na}$ (sodium), $I_{\rm K}$ (potassium), and I_L (leakage) evolve according to the following equations

$$I_T = g_{\rm Ca} m_T^2 h_T (V - E_{\rm Ca}), \quad I_L = g_L (V - E_L),$$
$$I_{\rm Na} = g_{\rm Na} m^3 h (V - E_{\rm Na}), \quad I_K = g_k n^4 (V - E_k),$$

which depend on V, on the intracellular calcium concentration Ca and on a set of further state variables (called *gating variables*) h, m, n, m_T, h_T. The differential equations governing these gating variables have the common structure written above (for the generic gating variable y), where

$$y^\infty = a_y/(a_y + b_y), \quad \tau_y = 1/(a_y + b_y) \quad (y = \{h, m, n\})$$
$$a_h = 0.128 e^{\frac{17-V}{18}}, \quad b_h = \frac{4}{e^{-0.2(V-40)}+1},$$
$$a_m = \frac{0.32(13-V)}{e^{0.25(13-V)}-1}, \quad b_m = \frac{0.28(V-40)}{e^{0.2(V-40)}-1},$$
$$a_n = \frac{0.032(15-V)}{e^{0.2(15-V)}-1}, \quad b_n = 0.5 e^{\frac{10-V}{40}},$$
$$m_T^\infty = \frac{1}{1+e^{-\frac{V+52}{7.4}}}, \quad \tau_{mT} = 0.44 + \frac{0.15}{e^{\frac{V+27}{10}} + e^{-\frac{V+102}{15}}},$$
$$h_T^\infty = \frac{1}{1+e^{\frac{V+80}{5}}}, \quad \tau_{hT} = 62.7 + \frac{0.27}{e^{\frac{V+48}{4}} + e^{-\frac{V+407}{50}}}.$$

In the above equations, h and m are the inactivation and activation variables of the Na^+ current; n is the activation variable of the K^+ current; m_T and h_T are the activation and inactivation variables of the low-threshold Ca^{2+} current; the leakage current I_L has conductance $g_L = 0.05\,[\frac{\rm mS}{\rm cm^2}]$ and reversal potential $E_L = -78\,[{\rm mV}]$; $I_{\rm Na}$ and $I_{\rm K}$ are the fast Na^+ and

TABLE I. Parameter values. Notice that for columns C and D the synaptic conductances are expressed in nS instead of nS/cm^2.

	A	B	C	D	E
α^{ex} [kHz]	0.1556	—	10	10	0.5
β^{ex} [kHz]	0.005	—	0.26	26	0.0005
θ^{ex} [mV]	25	−30	−40	−40	−42
g^{ex} [nS/cm^2]	0.0005	0.00001	1	0.4	0.0001
E^{ex} [mV]	60	60	20	20	50
α^{in} [kHz]	—	0.5	—	—	—
β^{in} [kHz]	—	0.02	—	—	—
θ^{in} [mV]	−30	25	−48.5	−48.5	−53
g^{in} [nS/cm^2]	0.0005	0.01	0.6	0.1	0.0001
E^{in} [mV]	−80	−80	−110	−110	−80
ν [mV^{-1}]	10	10	10	10	10

K^+ currents responsible for the generation of action potentials, with conductances $g_{\text{Na}} = 100\,[\frac{\text{mS}}{\text{cm}^2}]$ and $g_k = 10\,[\frac{\text{mS}}{\text{cm}^2}]$ and reversal potentials $E_{\text{Na}} = 50\,[\text{mV}]$ and $E_k = -95\,[\text{mV}]$; I_T is the low-threshold Ca^{2+} current that mediates the rebound burst response, with conductance $g_{\text{Ca}} = 1.75\,[\frac{\text{mS}}{\text{cm}^2}]$ and reversal potential $E_{\text{Ca}} = k_0 \frac{RT}{2F} \log(\frac{\text{Ca}_0}{\text{Ca}})$; I^{syn} is the synaptic current [Eq. (2) in the paper].

When the control current I_c is in the range $[-0.43, 0.13]\,[\frac{\mu\text{A}}{\text{cm}^2}]$ the neuron exhibits bursting behavior. The other parameters are set as follows: $C = 1\,[\frac{\mu F}{\text{cm}^2}]$, $\text{Ca}_0 = 2\,[\text{mM}]$, $d = 1\,[\mu\text{m}]$, $K_T = 0.0001\,[\text{mM ms}]$, $K_d = 0.0001\,[\text{mM}]$. $F = 96.489\,[\frac{C}{\text{mol}}]$ is the Faraday constant, $R = 8.31441\,[\frac{J}{\text{mol}\,K}]$ is the universal gas constant and the temperature T is set at 309.15 $[K]$.

2. Exponential integrate and fire neuron model

The exponential integrate and fire (eIF) neuron model [41] is defined by the following state equations:

$$\begin{aligned} \frac{dV}{dt} &= \frac{-g_L(V - E_L) + g_e e^{\frac{V - V_T}{\Delta_T}} - u + I_{\text{ext}} + I^{\text{syn}}}{C} \\ \frac{du}{dt} &= \frac{a(V - E_L) - u}{\tau_w} \end{aligned} \tag{A2}$$

where V is the membrane potential of the neuron; u is the adaptation variable; $g_L = 30\,[\text{nS}]$ is the leakage conductance and $E_L = -70.6\,[\text{mV}]$ is the leakage reversal potential; I^{syn} is the synaptic current [Eq. (2) in the paper].

When the conductance g_e is set at 110 [nS], the external current I_{ext} is varied in the range $[690, 1110]\,[\text{pA}]$ (Fig. 5). When the external current I_{ext} is set at $800\,[pA]$, the conductance g_e is varied in the range $[20, 160]\,[\text{nS}]$ (Fig. 6). For this range of parameter values, the neuron exhibits bursting behavior. The other parameters are set as follows: $C = 2007.4\,[pF]$, $V_T = -50.4\,[\text{mV}]$, $\Delta_T = 2\,[\text{mV}]$, $\tau_w = 285.7\,[\text{ms}]$, $a = 4\,[\text{nS}]$.

3. Plant neuron model

The Plant neuron model [39,40] is defined by the following state equations:

$$\begin{aligned} \frac{dV}{dt} &= \frac{-I_T - I_L - I_{\text{Na}} - I_{\text{K}} - I_{\text{KCa}} + I_{\text{ext}} + I^{\text{syn}}}{C}, \\ \frac{d\text{Ca}}{dt} &= \rho[K_c x(V_{\text{Ca}} - V) - \text{Ca}], \\ \frac{dy}{dt} &= \frac{y^\infty - y}{\tau_y} \quad y = \{h, n, x\}, \end{aligned} \tag{A3}$$

where

$$I_T = g_T x(V - E_I), \quad I_L = g_L(V - E_L), \quad I_{\text{Na}} = g_I m_\infty^3 h(V - E_I), \quad I_K = g_K n^4(V - E_K), \quad I_{\text{KCa}} = g_{K\text{Ca}} \frac{\text{Ca}}{\text{Ca} + 0.5}(V - E_K),$$

$$m_\infty = \frac{\frac{0.1(50 - V_s)}{e^{\frac{50 - V_s}{10}}}}{\frac{0.1(50 - V_s)}{e^{\frac{50 - V_s}{10}}} + 4e^{\frac{25 - V_s}{18}}}, \quad h^\infty = \frac{0.07e^{\frac{25 - V_s}{20}}}{0.07e^{\frac{25 - V_s}{20}} + \frac{1}{1 + e^{\frac{55 - V_s}{10}}}}, \quad \tau_h = \frac{12.5}{0.07e^{\frac{25 - V_s}{20}} + \frac{1}{1 + e^{\frac{55 - V_s}{10}}}}, \quad n^\infty = \frac{\frac{0.01(55 - V_s)}{e^{\frac{55 - V_s}{10}}} - 1}{\frac{0.01(55 - V_s)}{e^{\frac{55 - V_s}{10}}} - 1 + 0.125e^{\frac{45 - V_s}{80}}},$$

$$\tau_n = \frac{12.5}{\frac{0.01(55 - V_s)}{e^{\frac{55 - V_s}{10}}} - 1 + 0.125e^{\frac{45 - V_s}{80}}}, \quad x^\infty = \frac{1}{e^{0.15(-V - 50)} + 1}, \quad V_s = \frac{127V}{105} + \frac{8265}{105},$$

where V is the membrane potential of the neuron; Ca is the intracellular calcium concentration; x is the activation variable of the slow inward Ca^{2+} current; h is the inactivation variable of the Na^+ current; n is the activation variable of the K^+ current; I_L is the leakage current, with conductance $g_L = 0.003\,[\frac{\text{nS}}{\text{cm}^2}]$ and reversal potential $E_L = -40\,[\text{mV}]$; I_{Na} and I_{K} are the fast inward Na^+ and outward K^+ currents, respectively, with conductances $g_I = 8\,[\frac{\text{nS}}{\text{cm}^2}]$ and $g_K = 1.3\,[\frac{\text{nS}}{\text{cm}^2}]$ (these values ensure undershoot, see Fig. 4) and reversal potentials $E_I = 30$ mV and $E_K = -75\,[\text{mV}]$; I_T is the slow inward tetrodotoxin-resistant Ca^{2+} current, with conductance $g_T = 0.01\,[\frac{\text{nS}}{\text{cm}^2}]$ and reversal potential $E_T = 30\,[\text{mV}]$; I_{KCa}

is the outward Ca^{2+} sensitive K^+ current, with conductance $g_{KCa} = 0.03\,[\frac{nS}{cm^2}]$ and reversal potential E_K; I^{syn} is the synaptic current [Eq. (2)].

The external current I_{ext} is set to $0.028\,[\frac{\mu A}{cm^2}]$. The other parameters are set as follows: $C = 1\,[\frac{\mu F}{cm^2}]$, $\rho = 0.00015\,[mV^{-1}]$, $K_c = 0.0085\,[mV^{-1}]$, $V_{Ca} = 140\,[mV]$, $\tau_x = 235\,[ms]$.

APPENDIX B: SYNAPSE PARAMETER VALUES

In Table I, column A lists the parameter values used for the gHCO with the thalamic reticular neuron model, first-order dynamic excitatory synapses and static inhibitory synapses (Figs. 2 and 3). Column B lists the parameter values used when simulating the gHCO with the thalamic reticular neuron model, modified first-order dynamic inhibitory synapses [Eq. (5)] and static excitatory synapses (Figs. 7 and 8 in the paper). Column C lists the parameter values used for the gHCO with the eIF neuron model when varying I_{ext}, first-order dynamic excitatory synapses and static inhibitory synapses (Fig. 5). Column D lists the parameter values used for the gHCO with the eIF neuron model when varying g_e, first-order dynamic excitatory synapses and static inhibitory synapses (Fig. 6). Column E lists the parameter values used for the gHCO with the Plant neuron model, first-order dynamic excitatory synapses and static inhibitory synapses (Fig. 4).

[1] R. M. Harris-Warrick and J.-M. Ramirez, in *Neurobiology of Motor Control* (Wiley, New York, 2017), Chap. 8, pp. 225–262.
[2] O. Kiehn and K. Dougherty, in *Neuroscience in the 21st Century* (Springer, Berlin, 2016), pp. 1337–1365.
[3] P.-L. Buono and M. Golubitsky, J. Math. Biol. **42**, 291 (2001).
[4] C. M. Pinto and M. Golubitsky, J. Math. Biol. **53**, 474 (2006).
[5] A. J. Ijspeert, Neur. Netw. **21**, 642 (2008).
[6] J. Yu, M. Tan, J. Chen, and J. Zhang, IEEE Trans. Neural Netw. Learn. Syst. **25**, 441 (2013).
[7] S. M. Danner, N. A. Shevtsova, A. Frigon, and I. A. Rybak, Elife **6**, e31050 (2017).
[8] Y. I. Molkov, B. J. Bacak, A. E. Talpalar, and I. A. Rybak, PLoS Comp. Biol. **11** e1004270 (2015).
[9] M. Lodi, A. Shilnikov, and M. Storace, IEEE Trans. Circ. Syst. **65**, 1028 (2018).
[10] J. Ausborn, A. C. Snyder, N. A. Shevtsova, I. A. Rybak, and J. E. Rubin, J. Neurophysiol. **119**, 96 (2018).
[11] S. Grillner, Neuron **52**, 751 (2006).
[12] K. Takakusaki, Mov. Disord. **28**, 1483 (2013).
[13] V. Caggiano, R. Leiras, H. Goñi-Erro, D. Masini, C. Bellardita, J. Bouvier, V. Caldeira, G. Fisone, and O. Kiehn, Nature **553**, 455 (2018).
[14] M. Lodi, A. L. Shilnikov, and M. Storace, IEEE Trans. Neural Netw. Learn. Syst. **31**, 3658 (2020).
[15] T. G. Brown, J. Physiol. **48**, 18 (1914).
[16] R. L. Calabrese, Half-center oscillators underlying rhythmic movements, *The Handbook of Brain Theory and Neural Networks* (MIT Press, Cambridge, MA, 1998), pp. 444–447.
[17] T. Bem and J. Rinzel, J. Neurophysiol. **91**, 693 (2004).
[18] R. C. Elson, A. I. Selverston, H. D. Abarbanel, and M. I. Rabinovich, J. Neurophysiol. **88**, 1166 (2002).
[19] T. J. Lewis and J. Rinzel, J. Comput. Neurosci. **14**, 283 (2003).
[20] J. A. White, C. C. Chow, J. Rit, C. Soto-Treviño, and N. Kopell, J. Comput. Neurosci. **5**, 5 (1998).
[21] A. Doloc-Mihu and R. L. Calabrese, J. Biol. Phys. **37**, 263 (2011).
[22] N. Dale and A. Roberts, J. Physiol. **363**, 35 (1985).
[23] M. Pinco and A. Lev-Tov, J. Neurophysiol. **72**, 2406 (1994).
[24] C. Gunaratne, A. Sakurai, and P. S. Katz, J. Neurophysiol. **118**, 1123 (2017).
[25] A. Sakurai and P. S. Katz, J. Neurosc. **39**, 6460 (2019).
[26] E. M. Izhikevich, Int. J. Bifurcat. Chaos **10**, 1171 (2000).
[27] A. Destexhe, D. Contreras, T. J. Sejnowski, and M. Steriade, J. Neurophysiol. **72**, 803 (1994).
[28] R. Nagornov, G. Osipov, M. Komarov, A. Pikovsky, and A. Shilnikov, Commun. Nonlinear Sci. **36**, 175 (2016).
[29] X.-J. Wang, Neuroscience **89**, 347 (1999).
[30] D. V. Buonomano, J. Neurosc. **20**, 1129 (2000).
[31] S. Jalil, I. Belykh, and A. Shilnikov, Phys. Rev. E **85**, 036214 (2012).
[32] D. Somers and N. Kopell, Biol. Cybern. **68**, 393 (1993).
[33] S. Jalil, D. Allen, J. Youker, and A. Shilnikov, Chaos **23**, 046105 (2013).
[34] J. Wojcik, J. Schwabedal, R. Clewley, and A. L. Shilnikov, PloS One **9** e92918 (2014).
[35] L. Zhao and A. Nogaret, Phys. Rev. E **92**, 052910 (2015).
[36] C. Bellardita and O. Kiehn, Curr. Biol. **25**, 1426 (2015).
[37] M. Lemieux, N. Josset, M. Roussel, S. Couraud, and F. Bretzner, Front. Neurosci. **10**, 42 (2016).
[38] M. Lodi, A. Shilnikov, and M. Storace, in *Proceedings of the IEEE International Symposium on Circuits and Systems* (IEEE, Piscataway, NJ, 2017), pp. 1–4, https://doi.org/10.1109/ISCAS.2017.8050580.
[39] R. E. Plant, J. Math. Biol. **11**, 15 (1981).
[40] D. Alaçam and A. Shilnikov, Int. J. Bifurcat. Chaos **25**, 1540003 (2015).
[41] R. Brette and W. Gerstner, J. Neurophysiol. **94**, 3637 (2005).
[42] C. Van Vreeswijk, L. Abbott, and G. B. Ermentrout, J. Comput. Neurosci. **1**, 313 (1994).